

Article

Study on the Desliming Performance of a Novel Hydrocyclone Sand Washer

Xinghua Yang ^{*}, Guanghui Yang, Peikun Liu , Xiaoyu Li, Lanyue Jiang and Jiashun Zhang

College of Mechanical and Electrical Engineering, Shandong University of Science and Technology, Qingdao 266590, China; yangguanghv@163.com (G.Y.); lpk710128@163.com (P.L.); lixy2018@sudst.edu.cn (X.L.); jianglanyue5@sudst.edu.cn (L.J.); zjs1158@163.com (J.Z.)

* Correspondence: skd992489@sudst.edu.cn

Abstract: A novel hydrocyclone sand washer featured by connecting a cylindrical hydrocyclone and a conical-cylindric hydrocyclone in series was developed to improve the poor grading performance in current machine-made sand processing technology. The former hydrocyclone with a flat bottom was designed to enhance the centrifugal intensity, thereby achieving the pre-grading of fine and coarse particles and ensuring the discharge of most fine mud particles from the overflow pipe. The latter hydrocyclone was designed to achieve the secondary fine separation and therefore reduce the content of fine particles in the underflow product. Firstly, the flow field inside the consecutive hydrocyclones was simulated using an RSM and VOF model. The DPM model was introduced to trace the particle motion trajectory and validate the feasibility of hydrocyclone separation. Then, the experimental study was performed using the control variable method, and the effects of the first-section overflow pipe diameter, the feeding rate, and the mud–sand mixing ratio on the desliming performance were examined. Results show that the content of particles with a diameter of below 75 μm in the second-section underflow drops significantly after the separation in the hydrocyclone sand washer. When the first-section overflow pipe diameter, the feeding rate, and the mud–sand mixing ratio are set to 34 mm, 60 kg/h and 1:1, respectively, the desliming rate of the novel hydrocyclone sand washer can reach 94.31% and the loss rate of quartz sand is only 1.28%.

Keywords: hydrocyclone sand washer; desliming performance; particle motion trajectory; loss rate of quartz sand



Citation: Yang, X.; Yang, G.; Liu, P.; Li, X.; Jiang, L.; Zhang, J. Study on the Desliming Performance of a Novel Hydrocyclone Sand Washer. *Separations* **2022**, *9*, 74. <https://doi.org/10.3390/separations9030074>

Academic Editor: Ronald Beckett

Received: 11 February 2022

Accepted: 11 March 2022

Published: 13 March 2022

Publisher's Note: MDPI stays neutral with regard to jurisdictional claims in published maps and institutional affiliations.



Copyright: © 2022 by the authors. Licensee MDPI, Basel, Switzerland. This article is an open access article distributed under the terms and conditions of the Creative Commons Attribution (CC BY) license (<https://creativecommons.org/licenses/by/4.0/>).

1. Introduction

Sand usage in concrete has increased significantly with the booming construction industry. Due to the growing shortage of river sand as a natural resource, it is necessary to seek a favorable substitute for natural sand [1–3]. Meanwhile, the increasingly high demands for environmental protection also set high requirements on devices, thereby promoting the rapid industry development of dry technology for sand production and wet methods for sand washing. However, the quality of the machine-made sand is far from the necessary requirements as the content of mud in the sand significantly affects its performance [4–7]. As the amount of mud in the sand has different degrees of harmful effects on the mechanical properties of concrete, it has been limited in various countries; for example in China its maximum limit is 10% [8,9].

In order to improve the quality of the machine-made sand, scholars all over the world have conducted a great deal of theoretical and experimental studies [10–12]. Shi et al. [13] adopted the fine-grinding water-quenched blast furnace slags as aluminosilicate materials and used air-cooled blast furnace slag to replace the alkali active mortar made from the full-volume slags, which can effectively reduce the mud content. Xu et al. [14] significantly improved the quality of machine-made sand by mixing it with river sand. Arulmoly et al. [15] have studied the way of mixing the machine-made sand with offshore sand.

However, there still certain shortcomings exhibited in the above methods, i.e., high energy consumption, low production, complex devices, and serious wear.

To improve the recovery of concentrates, most researchers have used various methods such as desliming, flotation and filtration during mineral separation. Han et al. [16,17] used flotation to greatly improve the recovery of chalcopyrite. Hydrocyclones have been widely used in processes such as desliming and flotation due to their simple structure, absence of moving parts and high separation efficiency [18–21]. Tao et al. [22] used hydrocyclones to remove the fine particles below 45 μm in the material, and verify its feasibility for carrying out fine-grained desliming and sorting. Although hydrocyclones have many advantages, they also have some defects such as small separation size range. For the separation of particles with complex working conditions, it is always difficult for a single-section hydrocyclone to meet the production demand of high-precision separation [23] due to the complex particle composition in the mechanism sand.

A single-section hydrocyclone can hardly satisfy the desliming requirements on machine-made sand. For this reason, this study connected a cylindrical hydrocyclone and a conical-cylindric hydrocyclone in series for grading treatment of the machine-made sand. The underflow port of the first-section hydrocyclone was connected to the inlet of the second-section hydrocyclone. To be specific, the former used the water as a medium and it was characterized by a tangential bottom, aiming to enhance the centrifugal intensity, thereby achieving the pre-grading of fine and coarse particles and ensuring the discharge of most fine-mud particles with the size of below 75 μm from the overflow port; the latter was to enhance the downward flowing resistance of fluid, which can achieve the secondary fine separation of materials and reduce the content of fine mud in the underflow product of the second-section hydrocyclone. It also ensured that the content of particles with the size of below 75 μm is less than 10%.

2. Materials and Methods

2.1. Hydrocyclone Sand Washer

Figure 1 displayed the structure of the hydrocyclone sand washer, from which it can be observed that the sand washer includes two sections. In the first-section hydrocyclone (cylindrical), a V-shape feeding groove and a tangential underflow pipe were set at the top of the hydrocyclone, while the overflow pipe and the tangential medium water inlet were set at the bottom. The second-section hydrocyclone (conical-cylindric) mainly consisted of the upper cylinder and the lower cone, in which the overflow port was set at the top of the cylinder and the underflow port was set at the bottom of the cone. The feeding inlet of the second-section hydrocyclone was connected with the underflow port of the first-section hydrocyclone. In order to facilitate the analysis of the variation law of the internal flow field in the hydrocyclone sand washer under different structural parameters, two characteristic sections were defined, respectively, near the overflow port of the first-section hydrocyclone ($Z_1, z = 120 \text{ mm}$) and at the lower section of overflow port of the second-section hydrocyclone ($Z_2, z = 485 \text{ mm}$), as shown in Figure 2.

As can be seen from the figure, waters enter into the first-section hydrocyclone along the tangential direction under certain pressure, and the fluid domains of some flow fields including outer and inner rotational flows can be generated in the first-section hydrocyclone. The quartz sand with mud is then fed by self-gravity from the V-shaped feeding groove. Due to the effects of density difference and pressure, most of the fine mud and a few of fine-graded quartz sand are discharged from the overflow port of the first-section hydrocyclone under the action of inner rotational flow; and then, some of the unseparated fine mud and a great amount of quartz sand move gradually towards the inclined top under the action of outer rotational flow and arrive at the underflow port of the first-section hydrocyclone. Under the residual pressure generated at the underflow port of the first-section hydrocyclone, the fine mud and the quartz sand are fed into the second-section hydrocyclone for fine separation. On account of different proportions of water, quartz sand and fine mud, some fine mud and a small amount of fine-graded quartz sand are

discharged from the overflow port of the second-section hydrocyclone, and therefore, high-quality quartz sand and a tiny amount of fine mud are discharged from the underflow port of the second-section hydrocyclone. Table 1 lists the main structural parameters of the hydrocyclone sand washer.

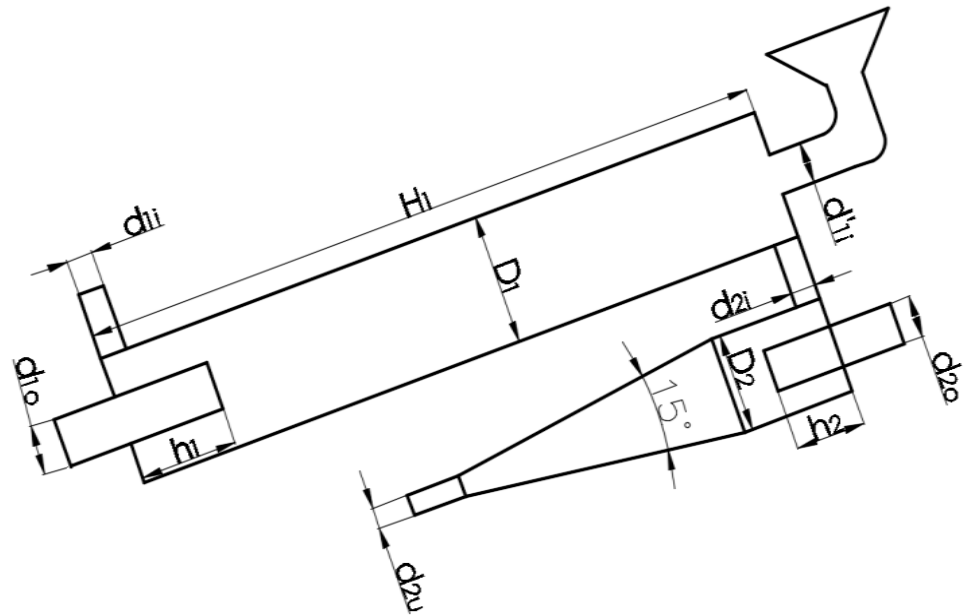


Figure 1. Illustration of the structure of the hydrocyclone sand washer.

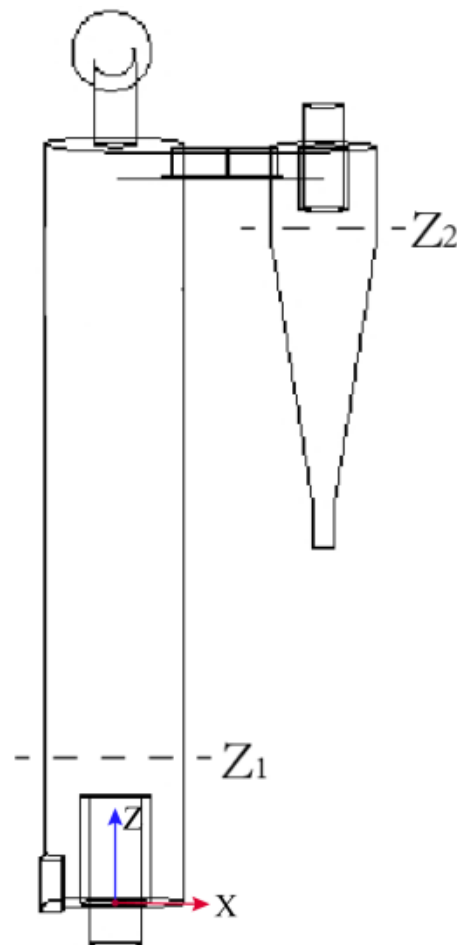


Figure 2. Location of feature lines.

Table 1. Main structural parameters of the hydrocyclone sand washer.

Section	Structural Parameter	Value/mm
The first-section hydrocyclone	Diameter of the column D_1	100
	Diameter of the water inlet d_{1i}	21
	Diameter of the overflow pipe d_{1o}	30, 34, 39
	Insert depth of the overflow pipe h_1	77
	Diameter of the feeding tube d'_{1i}	32
	Length of the column H_1	545
The second-section hydrocyclone	Equivalent diameter of the connecting tube between two sections d_{2i}	20
	Diameter of the column D_2	75
	Diameter of the overflow pipe d_{2o}	30
	Diameter of the underflow port d_{2u}	15
	Insert depth of the overflow pipe h_2	55
	Cone angle/ $^\circ$	15

2.2. Numerical Simulation

Although the structure of the hydrocyclone was simple, the internal flow field and particle movement were extremely complex [24–26]. Therefore, this study carried out a numerical simulation to simulate the internal flow field and particle trajectory, aiming to provide a theoretical basis for further experimental research. Taking the hydrocyclone sand washer as a research object, this study established a model and generated the hexahedral meshes with ICEM. After passing the independence test, the total number of meshes was determined as 1.44×10^5 , and the meshed results are shown in Figure 3. Using the FLUENT 19.0 software, two phases consisting of gas and liquid were simulated, in which the RSM model was selected as the turbulence model and the VOF model was used for multi-phase flow simulation. The inlet of water phase adopted ‘Velocity Inlet’ of 4 m/s. The overflow ports in the first- and second-sections, and the underflow port in the second-section were set as the ‘Pressure Outlet’. The backflow coefficient at the pressure outlet was set to one to ensure the air can enter into the hydrocyclone sand washer from at least an outlet.

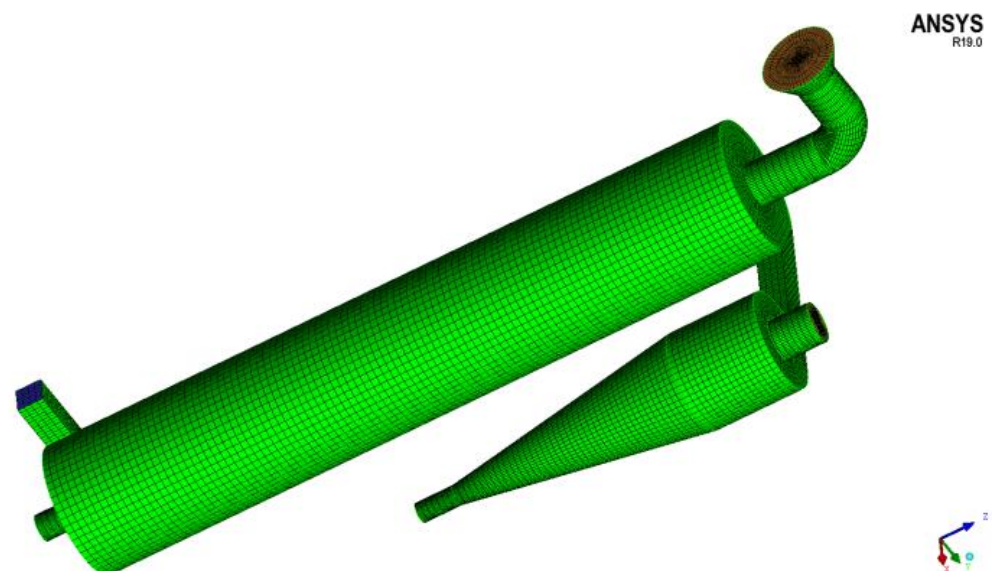


Figure 3. Mesh generation.

The wall surface followed the no-slip boundary conditions while the pressure-velocity coupled pattern and the pressure discrete pattern were described using the SIMPLE algorithm and PRESTO, respectively. The other control equations adopted the QUICK pattern with third-order precision to achieve fast convergence. The time step was set as 1×10^{-4} . The flow equilibrium between the outlet and inlet was set as the convergence basis. After

the simulation model reached convergence, the DPM model was introduced to trace the particle trajectory [27,28]. In this study, the motions of five different sizes of particles were simulated in the hydrocyclone sand washer to validate the applicability of the device.

2.2.1. RSM Model

The RSM model removes the assumption of isotropic vortex viscosity and establishes the Reynolds stress partial differential equation. The RSM model has better applicability for describing complex three-dimensional flows with strong cyclonic curves and strong rotation. The RSM control equation is shown in Equation (1):

$$\frac{\partial}{\partial t} (\overline{\rho u'_i u'_j}) + \frac{\partial}{\partial x_k} (\overline{\rho u'_i u'_j}) = D_{T,ij} + D_{L,ij} + P_{ij} + G_{ij} + \phi_{ij} + \varepsilon_{ij} + F_{ij} \quad (1)$$

Of which, the turbulent kinetic energy diffusion term:

$$D_{T,ij} = -\frac{\partial}{\partial x_k} [\overline{\rho u'_i u'_j u'_k} + \overline{p' u'_i \delta_{kj}} + \overline{p' u'_j \delta_{jk}}] \quad (2)$$

Molecular viscous diffusion term:

$$D_{L,ij} = \frac{\partial}{\partial x_k} \left[\mu \frac{\partial}{\partial x_k} (\overline{u'_i u'_j}) \right] \quad (3)$$

Shear stress generating term.

$$P_{ij} = \rho \left(\overline{u'_i u'_k \frac{\partial u_j}{\partial x_k}} + \overline{u'_j u'_k \frac{\partial u_i}{\partial x_k}} \right) \quad (4)$$

Buoyancy generation term.

$$G_{ij} = -\rho \beta (g_i \overline{u'_j \theta} + g_j \overline{u'_i \theta}) \quad (5)$$

Pressure strain terms.

$$\phi_{ij} = \overline{p' \left(\frac{\partial u'_i}{\partial x_j} + \frac{\partial u'_j}{\partial x_i} \right)} \quad (6)$$

Viscous dissipation term.

$$\varepsilon_{ij} = -2\mu \overline{\frac{\partial u'_i \partial u'_j}{\partial x_k \partial x_k}} \quad (7)$$

Rotational generation term for fluids.

$$F_{ij} = -2\rho \Omega_k (\overline{u'_j u'_m e_{ikm}} + \overline{u'_i u'_j e_{ikm}}) \quad (8)$$

2.2.2. VOF Model

The VOF model is a simplified Eulerian model for the solution of two-phase or multi-phase fluids that are mutually immiscible, and the simulated fluid domain space is filled by each phase of fluid. The size of the control volume occupied by each phase of fluid is the volume fraction of the simulated fluid domain, so the sum of the volume fraction is one. The formula is shown in Equation (9); by solving the continuous phase equation, the volume fraction of each phase changes sharply and the partition layer between the immiscible fluids is obtained.

$$\sum_{q=1}^n \alpha_q = 1 \quad (9)$$

Of which, α_q is the volume fraction of the q th phase within the fluid micro-element.

2.2.3. DPM Model

The DPM model uses the Euler-Lagrange method, which treats the fluid as the continuous phase and the solid particles as the discrete phase. It tracks the solid particle phase by setting up a force balance around the particle phase to obtain the particle motion trajectory, which can be written as

$$\frac{d\vec{u}_p}{dt} = \frac{\vec{u} - \vec{u}_p}{\tau_r} + \frac{\vec{g}(\rho_p - \rho)}{\rho_p} + \vec{F} \tag{10}$$

Of which, \vec{F} is an additional acceleration term and $\frac{\vec{u} - \vec{u}_p}{\tau_r}$ is the drag force per unit particle mass.

$$\tau_r = \frac{\rho_p d_p^2}{18\mu C_d Re} \tag{11}$$

Of which, τ_r is the particle relaxation time, \vec{u}_p is the particle velocity, \vec{u} is the fluid velocity, μ is the fluid viscosity, ρ is the fluid density, ρ_p is the particle density, d_p is the particle size, Re is the relative Reynolds number, and is given by

$$Re = \frac{\rho d_p |\vec{u}_p - \vec{u}|}{\mu} \tag{12}$$

2.3. Test Method

2.3.1. Test System

Figure 4 showed the scheme of the test system and photo of the hydrocyclone sand washer in the study. The whole device mainly consisted of the water sink, the pipe system, the submersible pump, the pressure gauge, the hydrocyclone sand washer, and the vibrating feeder. The hydrocyclone sand washer was arranged at an angle of 30° to the horizontal ground. Under normal temperature conditions, water was pumped into the hydrocyclone sand washer through the pipe system using the submersible pump, and the inlet water pressure was controlled at 0.10 MPa by adjusting the waterway switch. The vibrating feeder was installed on the top of the V-shaped feeding groove, controlling the feeding rate by adjusting the vibration frequency.

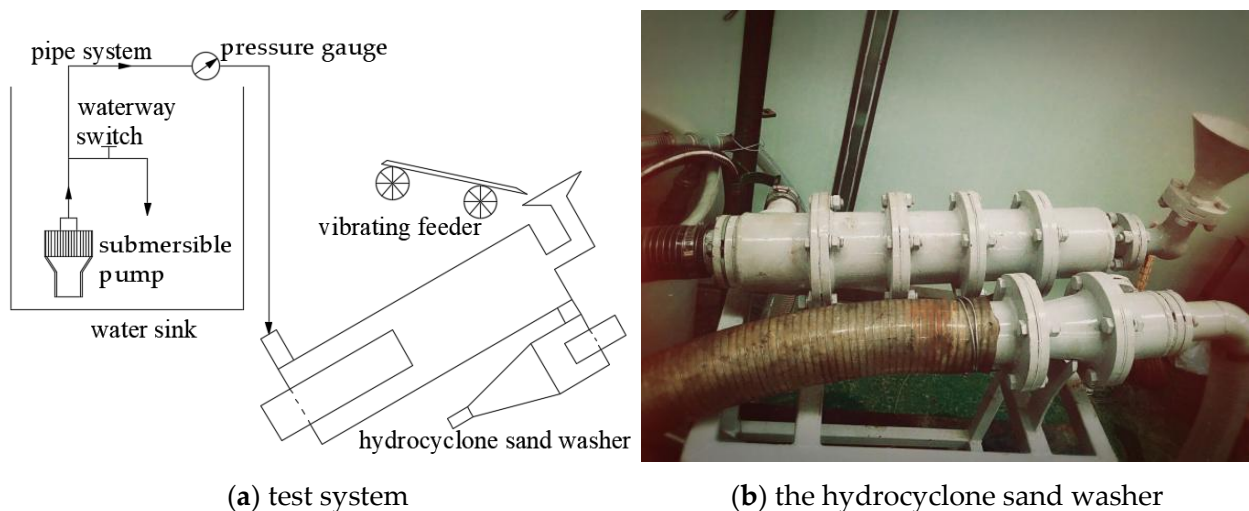


Figure 4. Scheme of the test system and photo of the hydrocyclone sand washer.

2.3.2. Test Mate Rials

In this study, the mud–sand mixture samples mainly composed of SiO₂ and CaCO₃ were used. The density of quartz sand for the experiment was 2650 kg/m³. After sieving, the particle sizes of quartz sand were measured, and the distributions were shown in Table 2. The particle sizes of the mixed mud were measured by a laser particle sizer BT-9300S, and the distributions were listed in Table 3.

Table 2. Distribution of particle sizes of quartz sand.

Particle Size (μm)	–25	25~75	75~100	100~150	150~200	200~250	250~300	+300
Mud content within the particle size range (%)	0.88	2.27	9.10	9.84	20.43	26.55	20.31	10.62
Negative accumulative contents (%)	0.88	3.15	12.25	22.09	42.52	69.07	89.38	100

Table 3. Distribution of particle sizes of mud.

Particle Size (μm)	–1	1~5	5~10	10~20	20~45	45~75	75~100	+100
Mud content within the particle size range (%)	2.26	20.90	13.56	19.61	27.23	13.08	2.92	0.44
Negative accumulative contents (%)	2.26	23.16	36.72	56.33	83.56	96.64	99.56	100

As shown in Table 2, in the quartz sand, the particles with a size below 75 μm occupied 3.15%, while the particles with a size between 75 and 100 μm occupied 9.10%, suggesting a large proportion of coarse particles in the quartz sand. From Table 3, in the mud, the particles with a size less than 45 μm occupied 83.56%, while the particles with a size less than 75 μm occupied 96.64%, suggesting a large proportion of fine particles in the mud. By combining Tables 2 and 3, it can be concluded that the quartz sand particles were coarser than the mud particles.

2.3.3. Test Design

Using the control variable method, the diameter of the first-section overflow port, the feeding rate, and the mud–sand mixing ratio were adjusted to explore the distribution rules and separation performances of the desliming effect of the developed hydrocyclone sand washer. Specifically, the diameters of the first-section overflow pipe were set to 30 mm, 34 mm and 39 mm, the mud–sand mixing ratios were set to 3:7, 2:3, 1:1, 3:2 and 7:3, and the feeding rates were controlled by adjusting the vibrating frequency of the vibrating feeder and set to 30 kg/h, 45 kg/h, 60 kg/h, 75 kg/h and 90 kg/h, respectively. When the hydrocyclone sand washer operated stably, materials were added and the sediments from the second-section underflow port were collected. After weighing the sediments via filtering and drying, the particle size distributions of the final products were analyzed by the laser particle sizer and then compared with the values of feeding materials, thereby calculating the desliming rate of the novel hydrocyclone sand washer and the loss rate of quartz sand.

3. Results and Discussion

3.1. Numerical Simulation and Analysis

3.1.1. Air Core

Figure 5 displays the forming process of the air core in the hydrocyclone sand washer at an inlet velocity of 4 m/s. Under certain pressure, water first entered into the first-section hydrocyclone along the tangential direction, then took the spiral rotation motion along an obliquely upward direction along the inner wall, and gradually moved towards the inside. The air at the center of the hydrocyclone sand washer decreased as fluid gradually filled the

hydrocyclone. At 2 s, a great amount of water entered into the second-section hydrocyclone and performed a rotation along the inner wall of the second-section hydrocyclone; as the fluid gradually filled the hydrocyclone, a great amount of air was discharged from the second-section overflow pipe, and the air core began to form. At 3.5 s, the flow field in the second-section hydrocyclone reached the stable state and a stable air core was formed; at the meantime, the flow field in the first-section hydrocyclone gradually tended to be stable and the air core began to form. At 4 s, the water flow rotated in the first-section hydrocyclone at a high speed and the inner air was gradually discharged from the first-section overflow pipe; the pressure at the center was gradually lower than atmospheric pressure, micro-pressure appeared at the feeding inlet, and the top air core gradually moved towards the feeding inlet. At 5 s, the flow field in the first-section hydrocyclone reached the stable state and formed a stable air core. It can be easily observed from the forming process of air cores in the hydrocyclone sand washer that, the air core in the second-section hydrocyclone was more rapidly formed than that in the first-section hydrocyclone.

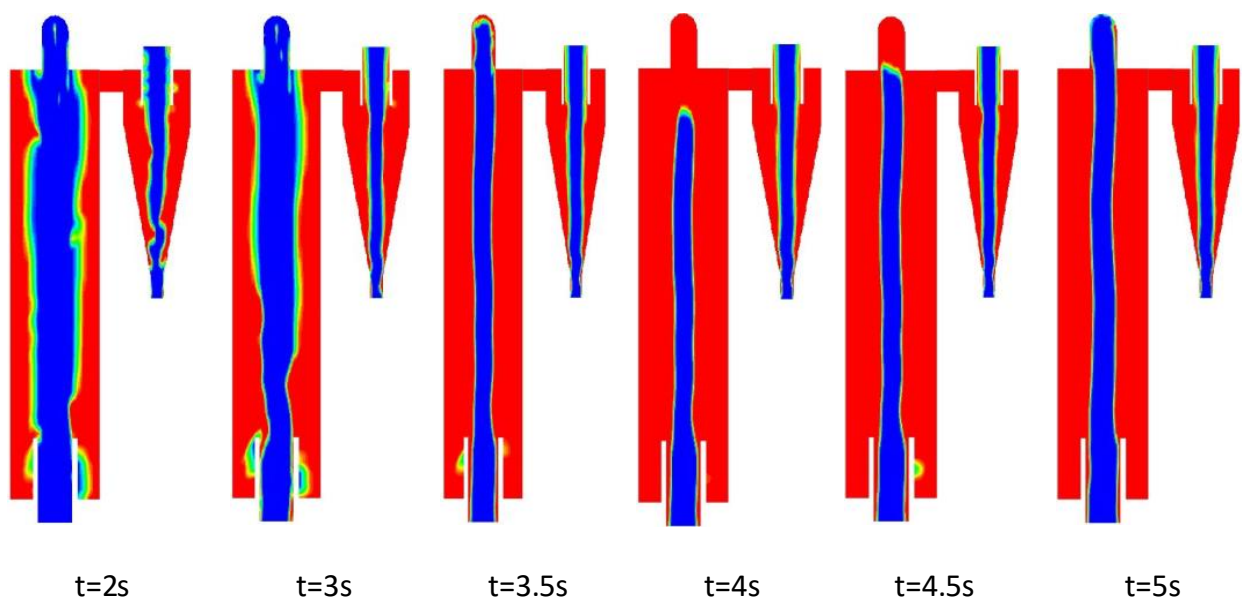


Figure 5. Illustration of the formation of air core in the hydrocyclone sand washer.

3.1.2. Axial Velocity

The axial velocity determines the residence time of the particles, and also has an important influence on the overflow and underflow rate, which in turn affects the separation effect. Figure 6 shows the axial velocity change law at Z_1 and Z_2 cross-section under the condition of different overflow pipe diameters of the first-section hydrocyclone. The positive and negative values represent the direction of the axial velocity. When the value is positive, the fluid flows towards the overflow port and forms the internal swirl; vice versa, when the value is negative, the fluid flows towards the underflow pipe and forms the external swirl. As can be seen from the graph, the axial velocity is negatively correlated with the overflow pipe diameter. As increasing the overflow pipe diameter, the axial velocity of the first-section hydrocyclone is significantly reduced, while the axial velocity of the second-section hydrocyclone show a slight reduction tendency. Therefore, when increasing the diameter of the overflow pipe, the axial velocity of the first-section hydrocyclone decreases, which is conducive to prolonging the time for the particles to enter the second-section hydrocyclone after a sufficient separation process. Thus, it is beneficial to reduce the content of fine-grained particles in the bottom flow and improve the desliming rate.

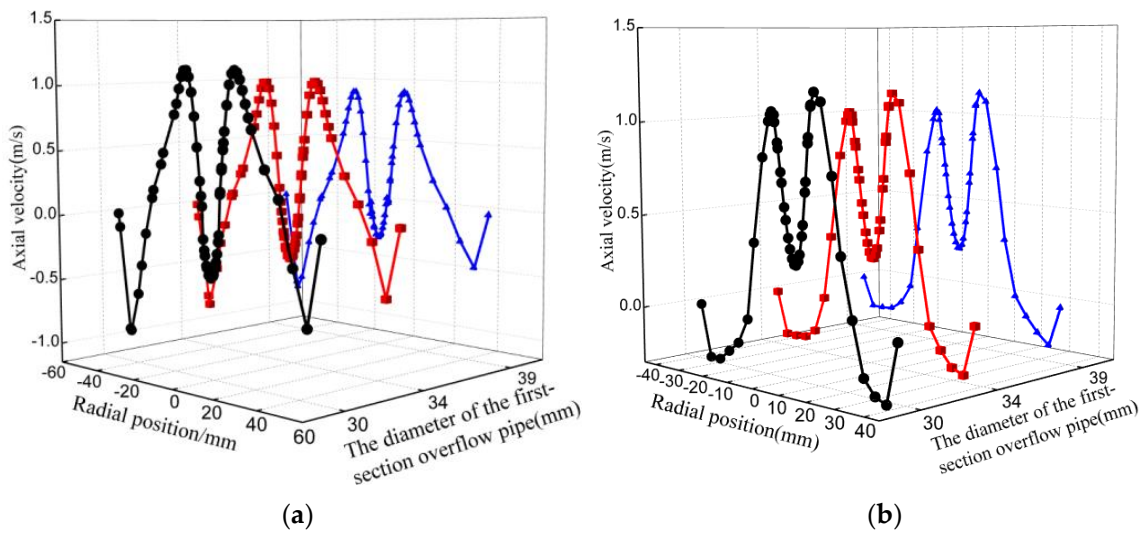


Figure 6. Effect of the first-section overflow pipe diameter on axial velocity (a) Cross-section of Z_1 ; (b) Cross-section of Z_2 .

3.1.3. Tangential Velocity

Figure 7 shows the variation law of the tangential velocity at Z_1 and Z_2 cross-section under the condition of different overflow pipe diameters of the first-section hydrocyclone. As can be seen from the figure, with the increase in the overflow pipe diameter, the maximum tangential velocity of both hydrocyclones decreases gradually. Compared to the first-section hydrocyclone, the tangential velocity of the second-section hydrocyclone decreases slightly. Also, the radial position of the maximum tangential velocity of the first-section hydrocyclone gradually migrates towards the wall as the overflow pipe diameter increases. The tangential velocity determines the strength of the centrifugal force field, which is the basic premise of cyclonic separation. In the process of particle separation, the stronger the centrifugal force field, the greater the centrifugal force on the particle, the easier it migrates into the outer swirl. Therefore, increasing the overflow pipe diameter of the first-section hydrocyclone reduces the tangential velocity, decreases the strength of the centrifugal force field and increases the separation size, which is not conducive to fine-grained sand entering the underflow. Obviously, it may lead to increasing sand loss rate in the underflow product.

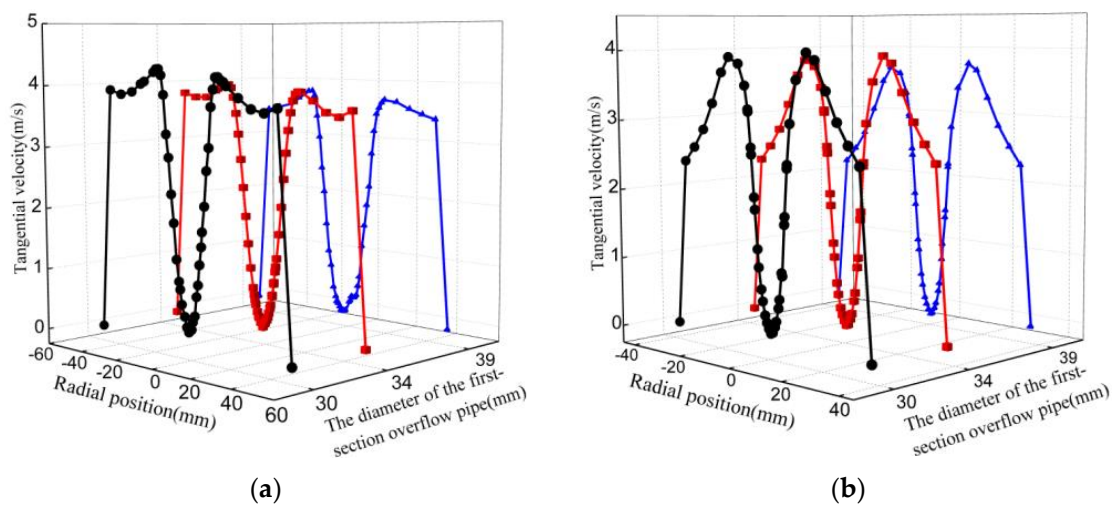


Figure 7. Effect of the first-section overflow pipe diameter on tangential velocity: (a) Cross-section of Z_1 ; (b) Cross-section of Z_2 .

From the trend of the axial velocity and the tangential velocity, it can be concluded that, although increasing the overflow pipe diameter of the first-section hydrocyclone is beneficial for extending the separation time of the particles, it may also reduce the strength of the centrifugal force field, leading to fine-grained sand loss in the underflow product.

3.1.4. Particle Motion Trajectory

In the simulation, five different sizes of particles were set at the feeding inlet to simulate the motion paths in the inner flow field, and the results were shown in Figure 8. As shown in Figure 8, the particles with a diameter of 25 μm were discharged from the overflow port of the first-section hydrocyclone; for the particles with a diameter of 45 μm , one part was discharged from the overflow port of the first-section hydrocyclone under the action of the inner rotational flow, and the other part entered into the second-section hydrocyclone under the action of the outer rotational flow and then discharged together with the particles with a diameter of 60 μm from the overflow port of the second-section hydrocyclone under the action of the inner rotational flow. This can be attributed to the formation of circulating flow at the end of the overflow pipe of the cylindrical hydrocyclone. The solid-phase particles can form a circulating fluidized bed in the circulating flow. Coarse particles can pass through the fluidized bed and enter into the outer rotational flow field; while fine particles cannot penetrate the fluidized bed and enter into the overflow in the first-section hydrocyclone via the inner rotational flow. As the particle size increased to 75 μm , particles can be discharged from the underflow port of the second-section hydrocyclone under the outer rotational flow in the conical-cylindric hydrocyclone. This is due to the fact that the lower part of the conical-cylindric hydrocyclone was an inverted cone, the sectional area gradually decreased downwards, the flow speed increased, accompanied with the enhanced centrifugal force field and the increase in particle downward resistance; accordingly, fine particles failed to overcome the resistance and discharged from the overflow port of the second-section hydrocyclone under the action of inner rotational flow, although coarse particles successfully overcame the resistance and entered into the underflow of the second-section hydrocyclone under the action of outer rotational flow. The simulation results of particle motion trajectories also validated the feasibility of the present hydrocyclone sand washing model.

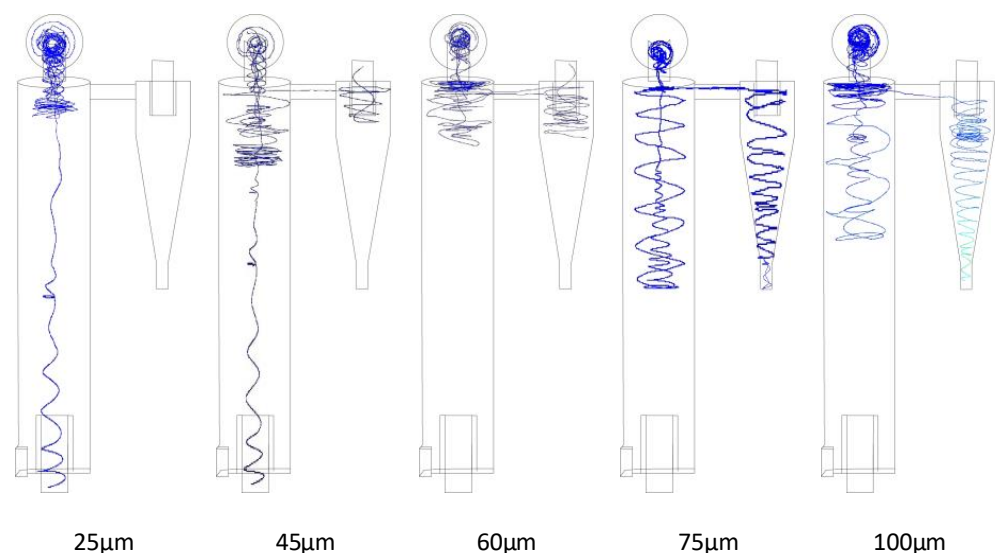


Figure 8. Trajectories of different particles in the hydrocyclone sand washer.

3.2. Test Results and Analysis

For analysis, taking the content of particles with a diameter below 75 μm in the overflow (the first-section overflow and the second-section overflow) as the desliming rate,

and the content of particles with a diameter of above 75 μm in the overflow as the loss rates of quartz sand.

3.2.1. Effects of the First-Section Overflow Pipe Diameter on the Desliming Performance

The diameter of the overflow pipe is an important structural parameter that affects the separation performance of the hydrocyclone sand washer. In the test, the mud–sand mixing ratio was set to 1:1, the feeding rate was set to 45 kg/h, and the diameter of the first-section overflow pipe was set to 30 mm, 34 mm and 39 mm, respectively. We calculated the particle size, the classification efficiency, the desliming rate and the quartz sand loss rate of the second-section underflow product under different overflow pipe diameter. The results were as shown in Table 4, Figures 9 and 10, respectively.

Table 4. Effect of the first-section overflow pipe diameter on cumulative particle size content.

Particle Size (μm)		−25	25~75	75~100	100~150	150~200	200~250	250~300	+300
The first-section overflow pipe diameter (mm)	30	8.15	10.46	21.46	30.41	56.69	80.61	94.32	100
	34	6.44	9.57	19.37	29.54	55.12	79.33	93.66	100
	39	5.65	9.24	18.75	28.12	51.95	75.12	93.32	100

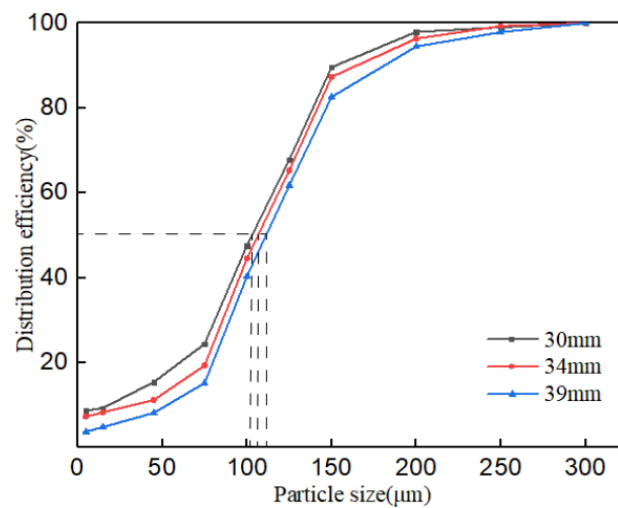


Figure 9. Effect of the first-section overflow pipe diameter on classification efficiency.

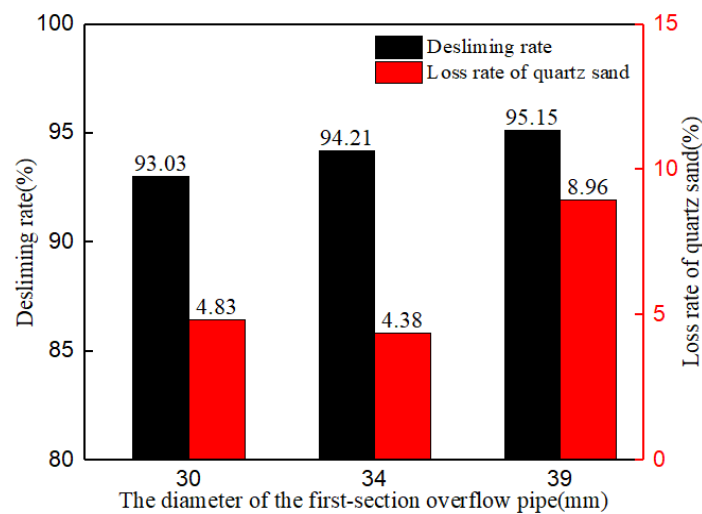


Figure 10. Influence of the first-section overflow pipe diameter on the desliming performance.

Table 4 shows the cumulative particle size content of the second-section underflow product at a different first-section overflow pipe diameter. It can be seen from the table, with the increase in the first-section overflow pipe diameter, the content of particles with a diameter of below 75 μm in the product gradually decreased by 1.22% from 10.46% to 9.24%. The content of particles with a diameter between 75 μm and 250 μm decreased by 4.27% from 70.15% to 65.88%, the content showed an obvious reduction tendency. While the content of particles with a diameter of above 250 μm showed a slow reduction tendency. When the first-section overflow pipe diameter was set to 30 mm, the content of particles with a diameter of below 75 μm of the second-section underflow was higher than 10%. As can be seen from Figure 9, the classification efficiency curve moved gradually towards the right with the increase in the first-section overflow pipe diameter, increasing the separation size and decreasing the content of fine particles in the underflow.

As shown in Figure 10, as the diameter of the overflow pipe increased from 30 mm to 39 mm, the desliming rate of the hydrocyclone sand washer increased gradually from 93.03% to 95.15%, and the loss rate of quartz sand increased by 4.13% from 4.83% to 8.96%.

This is due to the fact that, when the diameter of the first-section overflow pipe was small, the distribution amount of the first-section overflow decreased, and the centrifugal force field was stronger as a result of the larger tangential velocity, thereby increasing the centrifugal force on the particles. Under the action of the outer rotational flow, the probability of the fine-size particles entering into the second-section hydrocyclone increased, increasing the content of fine particles in the second-section underflow, leading to the low desliming rate. As the diameter of the first-section overflow pipe increased, the distribution amount of the first-section overflow increased, and the centrifugal force field was weaker due to the smaller tangential velocity. Although the phenomenon of fine particles mixed in the second-section underflow was alleviated, the probability of fine-grained quartz sand entering the first-section overflow increased, leading to more quartz sand loss. This result is in accordance with the simulated results shown in Figures 6 and 7. In this study, on the conditions of keeping the loss rate of quartz sand during the separation process as the top priority and simultaneously ensuring a certain desliming rate, we choose the 34 mm overflow pipe for the experiment.

3.2.2. Effects of the Feeding Rate on the Desliming Performance

The feeding rate was varied by adjusting the vibrating frequency of the vibrating feeder to derive the effects of the feeding rate on the desliming performance of hydrocyclone sand washer. As described above, the diameter of the first-section overflow pipe was determined as 34 mm through a comparison of the desliming performance. Next, using the materials with a mud–sand mixing ratio of 1:1, the simulation was performed when the feeding rates were set to 30 kg/h, 45 kg/h, 60 kg/h, 75 kg/h and 90 kg/h, respectively. The particle size, the classification efficiency, the desliming rate and the quartz sand loss rate of the second-section underflow product were calculated. The results were as shown in Table 5, Figures 11 and 12, respectively.

Table 5. Effect of the feeding speed on cumulative particle size content.

Particle Size (μm)		–25	25~75	75~100	100~150	150~200	200~250	250~300	+300
Feeding rate (kg/h)	30	5.24	8.13	18.16	31.74	56.54	81.65	93.75	100
	45	5.83	8.76	18.54	30.45	55.26	80.77	94.12	100
	60	6.44	9.57	19.37	29.54	55.12	79.33	93.66	100
	75	7.36	10.51	20.75	30.12	54.77	79.72	94.52	100
	90	9.12	13.22	23.32	31.44	55.32	80.13	95.88	100

As shown in Table 5 and Figure 11, with the increase in the feeding rate, the content of particles with a diameter of below 75 μm in the product gradually increased by 5.09% from 8.13% to 13.22%. In which, when the feeding rate increased from 75 kg/h to 90 kg/h, the content of particles below 75 μm in the second-section underflow increased by 2.71%,

which is the largest. In addition, the slope of the classification efficiency curve gradually decreased, indicating that the separation precision of the hydrocyclone sand washer gradually decreased. It can be seen from Table 5 that the content of 75 μm –200 μm particles in the second-section underflow gradually decreased by 6.31% from 48.41% to 42.10%, and the content of particles above 250 μm particles showed a slight reduction tendency, indicating that the recovery effect of the quartz sand gradually diminished.

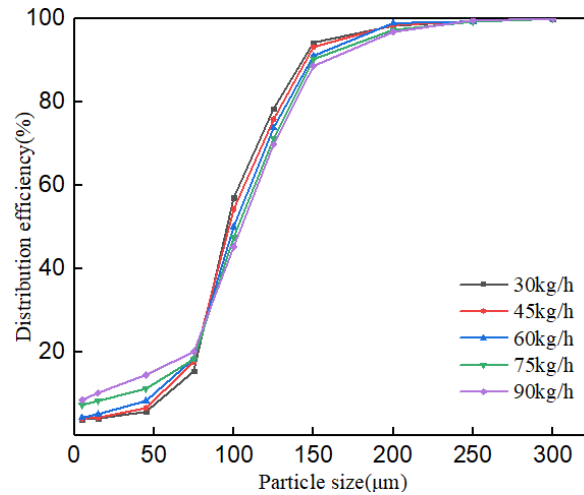


Figure 11. Effect of the feeding rate on classification efficiency.

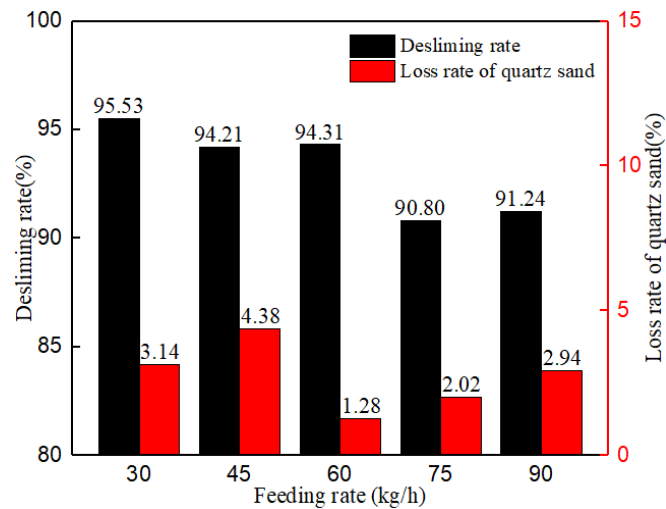


Figure 12. Effect of the feeding rate on the desliming performance.

As shown in Figure 12, with the increase in the feeding rate, the desliming rate of the hydrocyclone sand washer decreased gradually. As the feeding rate increased from 30 kg/h to 60 kg/h, the desliming rate decreased slightly by 1.22% from 95.53% to 94.31%; as the feeding rate further increased to 75 kg/h and 90 kg/h, the desliming rate dropped significantly by 3.51% to 90.80%, and the loss rate of quartz sand varied slightly. At a feeding rate of 45 kg/h, the loss rate of quartz sand was highest and reached up to 4.38%; at a feeding rate of 60 kg/h, the loss rate of quartz sand dropped to the minimum, 1.28%. The loss rate of quartz sand first decreased and then increased with the increasing feeding rate.

The separation process in the hydrocyclone sand washer includes not only the centrifugal sedimentation of solid particles under the action of water; it also includes the interference of interaction among particles. As the feeding rate increased, the concentration in material separation increased, more solid particles were processed in the hydrocyclone sand washer, both the density and viscosity of fluid increased, and the interference among

particles were enhanced, which increased energy consumption in the hydrocyclone separation process, gradually decreased the tangential velocity, and weakened the strength of the centrifugal force field and the separation precision. At a low feeding rate, the centrifugal force field was intensive, and particles separation precision was good enough. However, the concentration was low and some of the coarse particles will enter the overflow under the action of the fluid traction, leading to high loss rate of quartz sand; otherwise, at a high feeding rate, the separation process of the particles was not adequate, resulting in low desliming rate. Therefore, as the feeding rate increased, the desliming rate decreased gradually and the loss rate of quartz sand first decreased and then increased. In this study, under the operating condition of a high desliming rate, the loss rate of quartz sand should be the top priority and reduced to the lowest to ensure the reserve sand rate. The feeding rate was determined to 60 kg/h, and the desliming rate and the loss rate of quartz sand were 94.31 and 1.28%, respectively.

3.2.3. Effects of the Mud–Sand Mixing Ratio on the Desliming Performance

On account of different geological conditions among different regions, the mud contents also differ among different machine-made sand samples in the industrial sand washing process, thereby leading to the great fluctuation of desliming performance. In order to investigate the effects of the mud content of machine-made sand on the desliming performance, the separation performance was performed, during which the diameter of the first-section overflow pipe and the feeding rate were set as 34 mm and 60 kg/h according to the above test results, and the mud–sand mixing ratio was set to 3:7, 2:3, 1:1, 3:2 and 7:3, respectively. Calculating the particle size, the classification efficiency, the desliming rate and the quartz sand loss rate of the second-section underflow product under different mud–sand mixing ratio. The results were as shown in Table 6, Figures 13 and 14, respectively.

Table 6. Effect of the mud–sand mixing ratio on cumulative particle size content.

Particle Size (μm)	–25	25~75	75~100	100~150	150~200	200~250	250~300	+300
Mud–sand mixing ratio 3:7	4.17	7.34	20.45	30.54	58.08	80.15	94.12	100
2:3	5.22	8.98	19.36	30.13	56.17	79.58	93.89	100
1:1	6.44	9.57	19.37	29.54	55.12	79.33	93.66	100
3:2	8.73	11.04	19.25	28.35	53.36	75.35	92.00	100
7:3	9.12	14.24	22.43	27.33	51.69	73.25	92.23	100

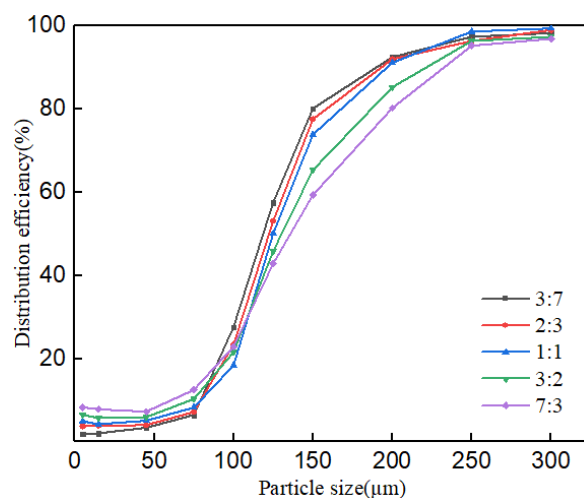


Figure 13. Effect of the mud–sand mixing ratio on classification efficiency.

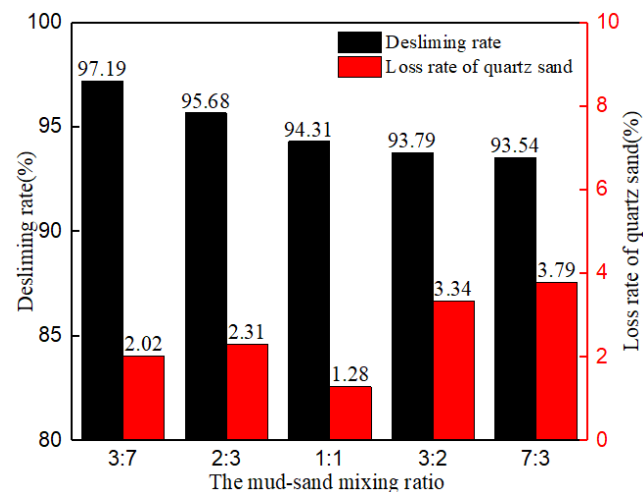


Figure 14. Effect of the mud–sand mixing ratio on desliming performance.

As can be seen from Table 6, with the increase in the mud–sand mixing ratio, the content of particles with a diameter of below 75 μm in the second-section underflow gradually increased by 6.90%, from 7.34% to 14.24%. Obviously, when the mud–sand mixing ratio is 3:2 or 7:3, the content of fine particles with a diameter of below 75 μm exceeded the required limit of 10%.

From Figure 13, when the mud–sand mixing ratio was 3:7, 2:3 and 1:1, the separation precision remained basically the same and the separation size increased slightly. However, when the mud–sand mixing ratio increased from 1:1 to 7:3, the content of particles with a diameter of above 75 μm in the second-section underflow increased significantly by 4.67%, indicating that the separation effect of the hydrocyclone sand washer gradually diminished. The slope of the classification efficiency curve tended to decrease overall, and the decreasing rate gradually increased, which proves this point. When the mud–sand mixing ratio increased from 3:7 to 7:3, the content of particles with a diameter between 75 μm and 250 μm in the second-section underflow gradually decreased, with a difference of 9.40% in the maximum value, and the content of particles with a diameter of above 250 μm changed weakly.

From Figure 14, the desliming rate decreased gradually with the increasing mud–sand mixing ratio in the materials. In particular, the desliming rate dropped significantly by 2.88% from 97.19% to 94.31% as the mixing ratio changed from 3:7 to 1:1, which decreased slightly by 0.77% as the mixing ratio changed from 1:1 to 7:3. The overall trend of loss rate of quartz sand first decreased and then increased, and reached the maximum 3.79% when the mud–sand mixing rate was 7:3. For the mixture with identical contents of mud and sand, the loss rate of sand was minimum, 1.28%.

This is due to the fact that, as the mud content in the sand increased, the content of fine-grained particles increased, and the concentration of material separation increased, leading to overall fine-grained particles in raw materials. The viscosity of the slurry increased and the particles were subjected to increasing fluid drag force. The enhanced interference among particles increased resistance for particles to enter the underflow. Accordingly, the desliming rate decreased and the loss rate of quartz sand increased. At a low mud content, the particles in raw materials were overall coarse, and the reducing slurry concentration made the interference among particles weaker, thereby contributing to the enhancement of desliming rate. Conclusively, as the mud content increased, the desliming performance of the hydrocyclone sand washer decreased gradually, and the loss rate of quartz sand first decreased and then increased.

3.2.4. Data Error Analysis

In order to exclude the errors brought by the experiment data to the result analysis, the variance analysis of the sample data measured during the experiment were analyzed,

as shown in Table 7. X_1 , X_2 and X_3 indicate the first-section overflow pipe diameter, the feeding rate and the mud–sand mixing ratio, respectively, Y_1 and Y_2 indicate the desliming rate and loss rate of quartz sand, respectively, and N_1 and N_2 indicate the data measured twice during the test, respectively. It can be seen that, the sample variance values for both Y_1 and Y_2 was small, indicating that the fluctuations in the sample data were small, so it is reasonable to use the mean value of the sample data in the analysis of the test results.

Table 7. Variance analysis of the experimental data.

X_1 (mm)	X_2 (kg/s)	X_3	Y_1 (%)				Y_2 (%)			
			N_1	N_2	Average	Variance	N_1	N_2	Average	Variance
30	75	1:1	92.75	93.31	93.03	0.0784	4.64	5.02	4.83	0.0361
34	75	1:1	94.01	94.41	94.21	0.0400	4.23	4.53	4.38	0.0225
39	75	1:1	95.01	95.29	95.15	0.0196	8.66	9.26	8.96	0.0900
34	30	1:1	95.41	95.65	95.53	0.0144	3.02	3.26	3.14	0.0144
34	45	1:1	94.25	94.37	94.31	0.0036	1.15	1.41	1.28	0.0169
34	60	1:1	90.51	91.09	90.80	0.0841	1.96	2.08	2.02	0.0036
34	90	1:1	91.11	91.37	91.24	0.0169	2.80	3.08	2.94	0.0196
34	75	3:7	97.10	97.28	97.19	0.0081	1.98	2.06	2.02	0.0016
34	75	2:3	95.44	95.92	95.68	0.0576	2.16	2.46	2.31	0.0225
34	75	3:2	93.70	93.88	93.79	0.0081	3.27	3.41	3.34	0.0049
34	75	7:3	93.46	93.62	93.54	0.0064	3.68	3.90	3.79	0.0121

4. Conclusions

In this study, a new type of hydrocyclone sand washer was proposed, which connected a cylindrical and a conical-cylindrical cyclone in series to conduct desliming experiments on mud–sand samples. Compared with the existing sand washing process, this simplified process avoids the pulping process and improves the production efficiency. Two-stage hydrocyclone separation can ensure high-efficiency desliming rate and low loss rate of quartz sand.

As the first-section overflow pipe diameter increased, the desliming rate of the hydrocyclone sand washer varied slightly, and the separation size increased gradually. As the first-section overflow pipe diameter increased from 30 mm to 34 mm, the loss rate of quartz sand varied slightly. The loss rate of quartz sand reached the maximum when first-section overflow pipe diameter was 39 mm.

As the feeding rate increased, the concentration of materials separation increased, while the desliming performance and the classification efficiency of the hydrocyclone sand washer decreased gradually. The desliming rate reached the maximum of 95.53% at the feeding rate of 30 kg/h, while the loss rate of quartz sand reached the optimum of 1.28% at the feeding rate of 60 kg/h.

As the mud content increased, the classification efficiency decreased gradually. The desliming rate decreased gradually, and the loss rate of quartz sand first decreased and then increased. At a mud–sand mixing ratio of 3:7, the desliming rate reached the optimum of 97.19%; at a mud–sand mixing ratio of 1:1, the loss rate of quartz sand dropped to the minimum of 1.28%.

Conclusively, in order to ensure the top priority of lowest loss rate of quartz sand and keep a high desliming rate, the diameter of the first-section overflow pipe, the feeding rate, and the mud–sand mixing ratio should be set to 34 mm, 60 kg/h, and 1:1, respectively. For ensuring as a top priority the highest desliming rate and for keeping a low loss rate of quartz sand, the diameter of the first-section overflow pipe, the feeding rate, and the mud–sand mixing ratio should be set to 34 mm, 30 kg/h, and 3:7, respectively.

Author Contributions: Conceptualization, X.Y. and P.L.; methodology, G.Y.; and L.J.; numerical simulation and experiments, G.Y. and J.Z.; validation, X.L.; data curation, J.Z.; writing—original

draft preparation, G.Y.; writing—review and editing, X.Y. All authors have read and agreed to the published version of the manuscript.

Funding: This research was funded by National Natural Science Foundation of China, grant number 22108159 and Natural Science Foundation of Shandong Province, China, grant number ZR2020ME105, ZR2021QB068.

Data Availability Statement: Not applicable.

Conflicts of Interest: The authors declare no conflict of interest.

References

1. Agrawal, U.S.; Wanjari, S.P.; Naresh, D.N. Characteristic study of geopolymers fly ash sand as a replacement to natural river sand. *Constr. Build. Mater.* **2017**, *150*, 681–688. [\[CrossRef\]](#)
2. Ren, Q.; Tao, Y.X.; Jian, D.W.; Ye, G.; De Schutter, G. Plastic viscosity of cement mortar with manufactured sand as influenced by geometric features and particle size. *Cem. Concr. Compos.* **2021**, *122*, 104163. [\[CrossRef\]](#)
3. Akhtar, M.N.; Ibrahim, Z.; Bunnori, N.M.; Jameel, M.; Tarannum, N.; Akhtar, J.N. Performance of sustainable sand concrete at ambient and elevated temperature. *Constr. Build. Mater.* **2021**, *280*, 122404. [\[CrossRef\]](#)
4. Chousidis, N.; Rakanta, E.; Ioannou, I.; Batis, G. Mechanical properties and durability performance of reinforced concrete containing fly ash. *Constr. Build. Mater.* **2015**, *101*, 810–817. [\[CrossRef\]](#)
5. Turk, K.; Demirhan, S. The mechanical properties of engineered cementitious composites containing limestone powder replaced by microsilica sand. *Can. J. Civ. Eng.* **2013**, *40*, 151–157. [\[CrossRef\]](#)
6. Khaleel, O.R.; Razak, H.A. The effect of powder type on the setting time and self compactability of mortar. *Constr. Build. Mater.* **2012**, *36*, 20–26. [\[CrossRef\]](#)
7. Turk, K.; Demirhan, S. Effect of limestone powder on the rheological, mechanical and durability properties of ECC. *Eur. J. Environ. Civ. Eng.* **2017**, *21*, 1157–1170. [\[CrossRef\]](#)
8. Chong, L.; Shi, C.J.; Yang, J.M.; Jia, H.F. Effect of limestone powder on the water stability of magnesium phosphate cement-based materials. *Constr. Build. Mater.* **2017**, *148*, 590–598. [\[CrossRef\]](#)
9. He, H.; Wang, Y.L.; Wang, J.J. Compactness and hardened properties of machine-made sand mortar with aggregate micro fines. *Constr. Build. Mater.* **2020**, *250*, 118828. [\[CrossRef\]](#)
10. Li, Y.R.; Zeng, X.H.; Zhou, J.L.; Shi, Y.; Umar, H.A.; Long, G.C.; Xie, Y.J. Development of an eco-friendly ultra-high performance concrete based on waste basalt powder for Sichuan-Tibet Railway. *J. Clean. Prod.* **2021**, *312*, 127775. [\[CrossRef\]](#)
11. Mao, X.Q.; Qu, W.; Zhu, P. Mixture optimization of green reactive powder concrete with recycled powder. *J. Mater. Civ. Eng.* **2019**, *31*, 04019033. [\[CrossRef\]](#)
12. Dobiszewska, M.; Schindler, A.K.; Pichor, W. Mechanical properties and interfacial transition zone microstructure of concrete with waste basalt powder addition. *Constr. Build. Mater.* **2018**, *177*, 222–229. [\[CrossRef\]](#)
13. Shi, J.; Tan, J.; Liu, B.; Chen, J.; Dai, J.; He, Z. Experimental study on full-volume slag alkali-activated mortars: Air-cooled blast furnace slag versus machine-made sand as fine aggregates. *J. Hazard. Mater.* **2020**, *403*, 123983. [\[CrossRef\]](#)
14. Xu, H.; Chen, X.; Dang, W.; Guo, X.; Guan, J.; Li, J. Technical application of machine-made sand in the production of the commercial concrete. *IOP Conf. Ser. Earth Environ. Sci.* **2021**, *647*, 012105. [\[CrossRef\]](#)
15. Arulmoly, B.; Konthesingha, C.; Nanayakkara, A. Performance evaluation of cement mortar produced with manufactured sand and offshore sand as alternatives for river sand. *Constr. Build. Mater.* **2021**, *297*, 123784. [\[CrossRef\]](#)
16. Han, G.; Wen, S.; Wang, H.; Feng, Q. Sulfidization regulation of cuprite by pre-oxidation using sodium hypochlorite as an oxidant. *Int. J. Min. Sci. Technol.* **2021**, *31*, 1117–1128. [\[CrossRef\]](#)
17. Han, G.; Wen, S.; Wang, H.; Feng, Q. Enhanced sulfidization flotation of cuprite by surface modification with hydrogen peroxide. *Trans. Nonferrous Met. Soc. China* **2021**, *31*, 3564–3578. [\[CrossRef\]](#)
18. Lim, E.W.C.; Chen, Y.R.; Wang, C.H.; Wu, R.M. Experimental and computational studies of multiphase hydrodynamics in a hydrocyclone separator system. *Chem. Eng. Sci.* **2010**, *65*, 6415–6424. [\[CrossRef\]](#)
19. Ni, L.; Tian, J.; Song, T.; Jong, Y.; Zhao, J. Optimizing geometric parameters in hydrocyclones for enhanced separations: A review and perspective. *Sep. Purif. Rev.* **2018**, *48*, 30–51. [\[CrossRef\]](#)
20. Ullmann, G.; Gonçalves, S.M.; Kyriakidis, Y.N.; de Souza Barrozo, M.A.; Vieira, L.G.M. Optimization study of thickener hydrocyclones. *Miner. Eng.* **2021**, *170*, 107066. [\[CrossRef\]](#)
21. Hou, D.X.; Cui, B.Y.; Zhang, H.; Zhao, Q.; Ji, A.K.; Wei, D.Z.; Feng, Y.Q. Designing the hydrocyclone with flat bottom structure for weakening bypass effect. *Powder Technol.* **2021**, *394*, 724–734. [\[CrossRef\]](#)
22. Tao, Y.J.; Zhao, Y.N.; Xian, Y.S.; Song, A.; Wang, Y.P.; Shi, Z.X. Coal Desliming Using Annular Rinse Water Hydrocyclone. *Key Eng. Mater.* **2020**, *4894*, 28–40. [\[CrossRef\]](#)
23. Lu, S.S.; Lu, X.J.; Yuan, Z.T.; Zhang, C.E.; Liu, J.T.; Liu, P.K.; Zhang, Y.K. The Beneficiation of fine coal by a combination of three-product cyclone and fine screen. *Int. J. Coal Prep. Util.* **2016**, *36*, 207–217. [\[CrossRef\]](#)
24. Mokni, I.; Dhaouad, H.; Bournot, P.; Mhiri, H. Numerical investigation of the effect of the cylindrical height on separation performances of uniflow hydrocyclone. *Chem. Eng. Sci.* **2015**, *122*, 500–513. [\[CrossRef\]](#)

25. Vega-Garcia, D.; Cilliers, J.J.; Brito-Parada, P.R. CFD modelling of particle classification in mini-hydrocyclones. *Sep. Purif. Technol.* **2020**, *251*, 117253. [[CrossRef](#)]
26. Ye, J.X.; Xu, Y.X.; Song, X.F.; Yu, J.G. Numerical modelling and multi-objective optimization of the novel hydrocyclone for ultra-fine particles classification. *Chem. Eng. Sci.* **2019**, *207*, 1072–1084. [[CrossRef](#)]
27. Li, F.; Liu, P.K.; Yang, X.H.; Zhang, Y.K.; Li, X.Y.; Jiang, L.Y.; Wang, H.; Fu, W.X. Purification of granular sediments from wastewater using a novel hydrocyclone. *Powder Technol.* **2021**, *393*, 751–763. [[CrossRef](#)]
28. Vakamalla, T.R.; Vadlakonda, B.; Aketi, V.A.; Mangadoddy, N. Multiphase CFD modelling of mineral separators performance: Validation against tomography data. *Trans. Indian Inst. Met.* **2017**, *70*, 323–340. [[CrossRef](#)]